Continuous-Flow Organic Electrosynthesis of a Conjugated Bipolar Polymer Cathode for High-Performance Low-Temperature Aqueous Aluminum-Ion Batteries

Longhai Zhang,[a] Cheng Ji,[a] Quanwei Ma,[a] Hongbao Li,[a] Rui Wang,[a] Lin Zhang,[b] Shilin Zhang,[c] Qingyu Yan,[d] Dongliang Chao,[e] Chaofeng Zhang*[a]

[a]*Institutes of Physical Science and Information Technology, Leibniz International Joint Research Center of Materials Sciences of Anhui Province, Anhui University, Hefei 230601, China.*
[b]*Institute for Solid State Physics, Leibniz University Hannover, Appelstrasse 2, Hannover 30167, Germany.*
[c]*School of Chemical Engineering, The University of Adelaide, Adelaide 5005, Australia.*
[d]*School of Materials Science and Engineering, Nanyang Technological University Singapore 637371, Singapore.*
[e]*Laboratory of Advanced Materials, Aqueous Battery Center, College of Smart Materials and Future Energy, Fudan University, Shanghai, 200433, P. R. China.*

* Corresponding author：E-mail: cfz@ahu.edu.cn

Experimental section

Prepare the pouch batteries

The assembly of pouch batteries follows a procedure similar to that of coin cells. The PDND/C cathode was prepared by mixing active material (60 wt%), ketjen Black (KB, 30 wt%), polyvinylidene fluoride (PVDF, 10 wt%), and then coating the mixture on the Ti sheets followed by drying. Subsequently, the pouch batterie was assembled with cathode, polished Al foil as anode (3cm * 3cm), glass fiber as the separator (Whatman, GF/A), and an aqueous electrolytes (1 M $Al(ClO_4)_3$).

Theoretical Specific Capacity

The theoretical specific capacity of the PDND cathode material can be obtained using the following equation:

$$Q_{spec} = \frac{n \cdot F}{3.6 \cdot M_w} = \frac{26801 \cdot n}{M_w}$$

where Mw is the relative molecular weight of the unit in PDND skeleton (188 g mol^{-1}), and n stands for the transferred electrons per unit (3-electron reaction). As a result, the theoretical capacity of the PDND cathode is calculated to be 427.7 mA h g^{-1}.

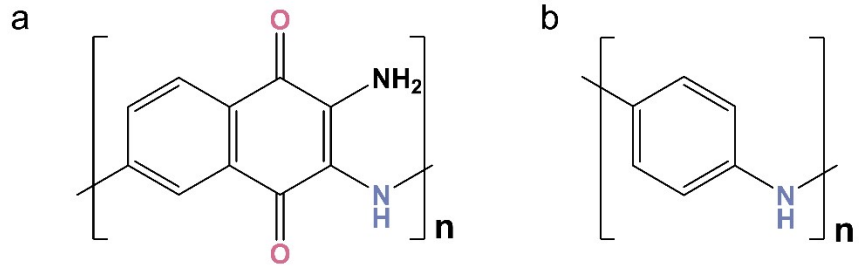

Figure S1. The molecular structures of (a) PDND and (b) PANI.

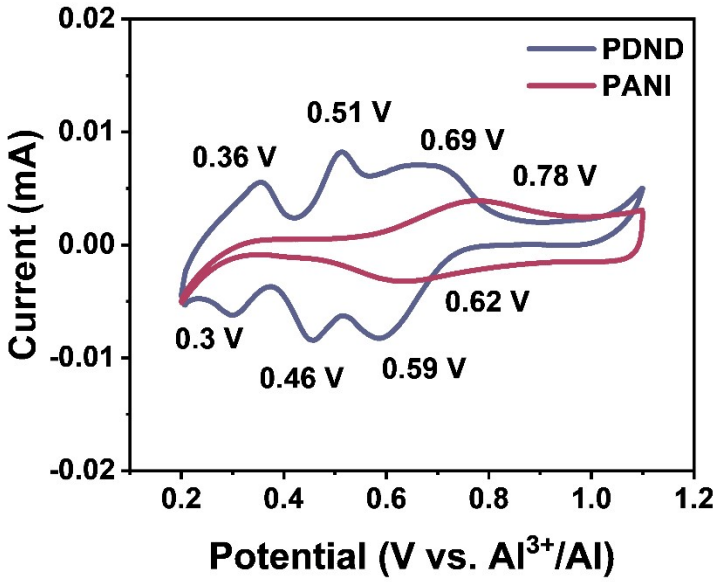

Figure S2. The CV curves of Al//PDND and Al//PANI batteries at 0.1 mV s^{-1}.

The increased number of redox peaks observed in the CV curve of PDND serves as evidence that the introduction of carbonyl functional groups effectively activates the multi-electron reaction.

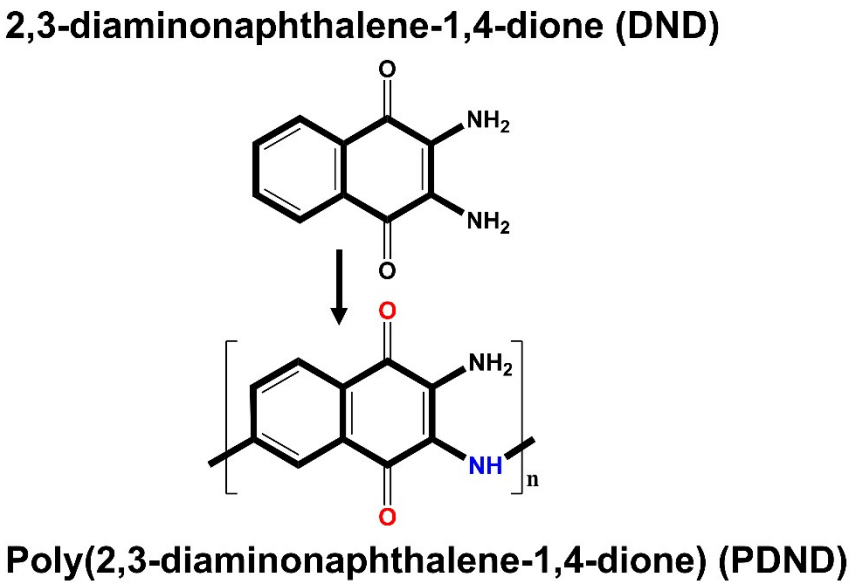

Figure S3. Illustration of the electrosynthesis process of PDND cathode.

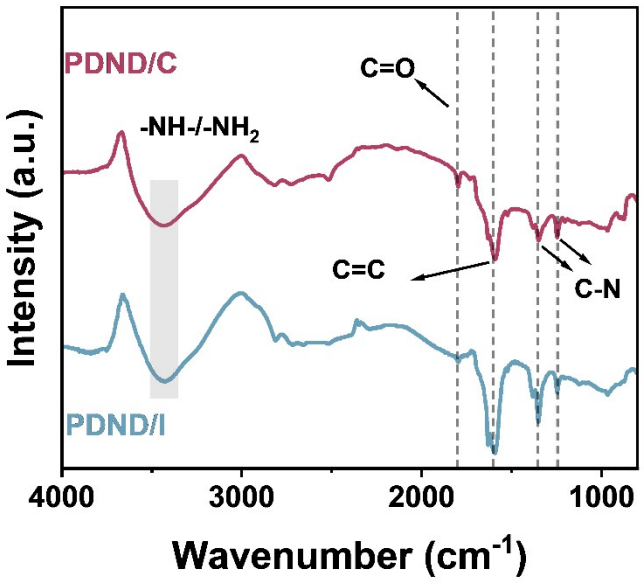

Figure S4. FT-IR of the PDND/C and PDND/I samples.

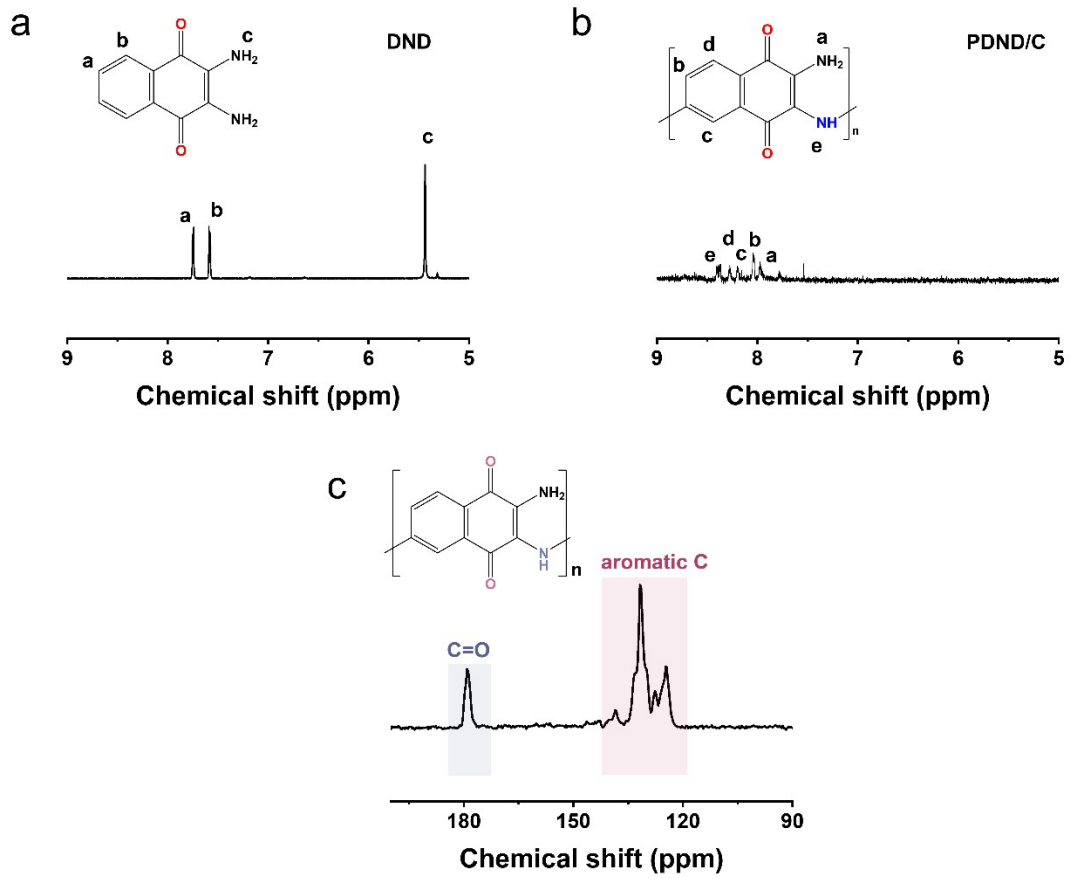

Figure S5. ^{1}H NMR spectra of (a) DND and (b) PDND. (c) ^{13}C NMR spectra of PDND.

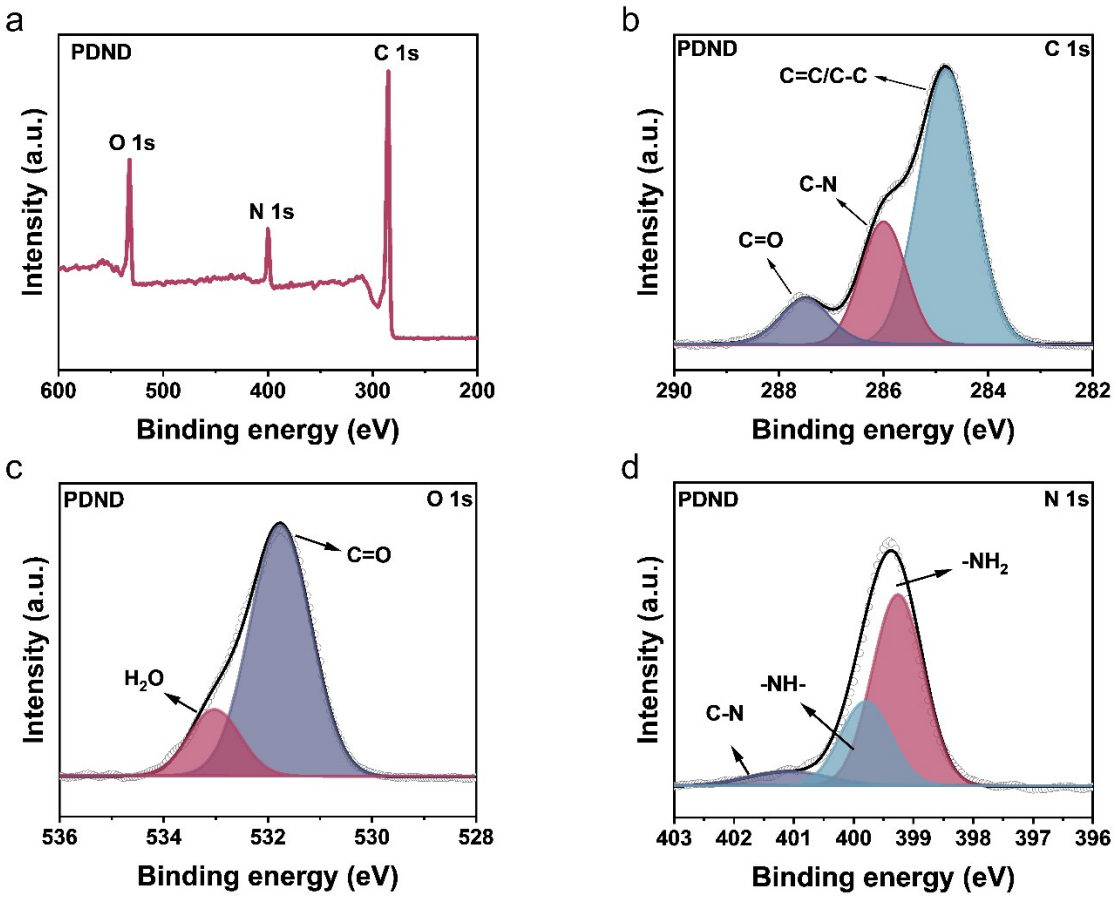

Figure S6. XPS survey spectrum of PDND.

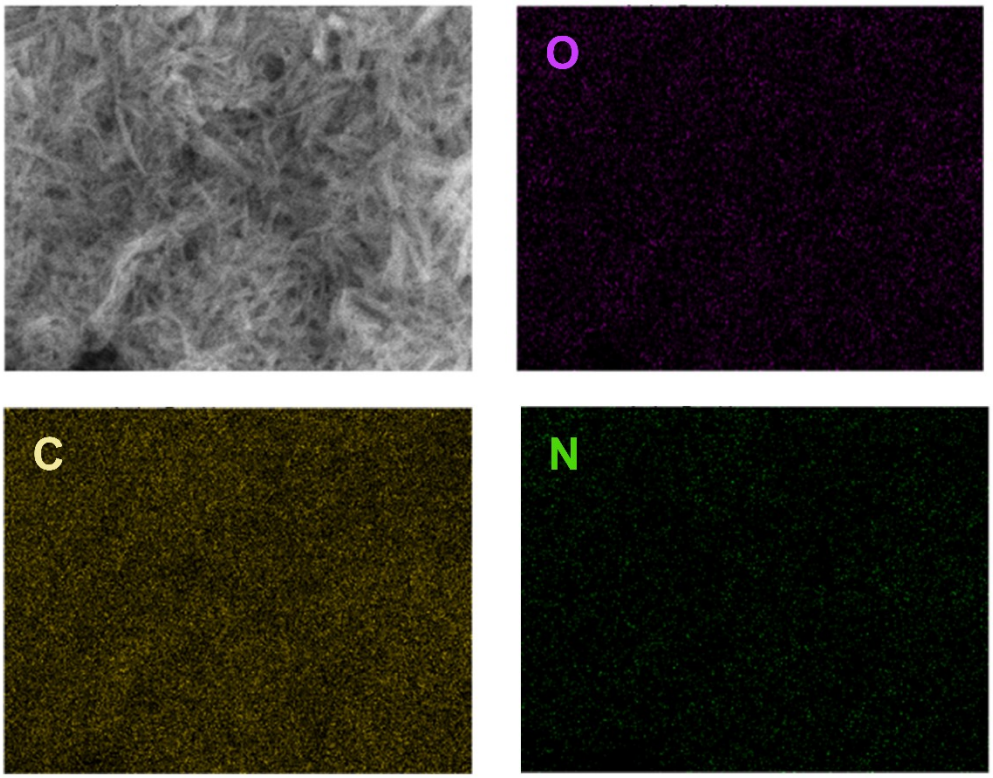

Figure S7. SEM and the corresponding EDS elemental mapping images of PDND.

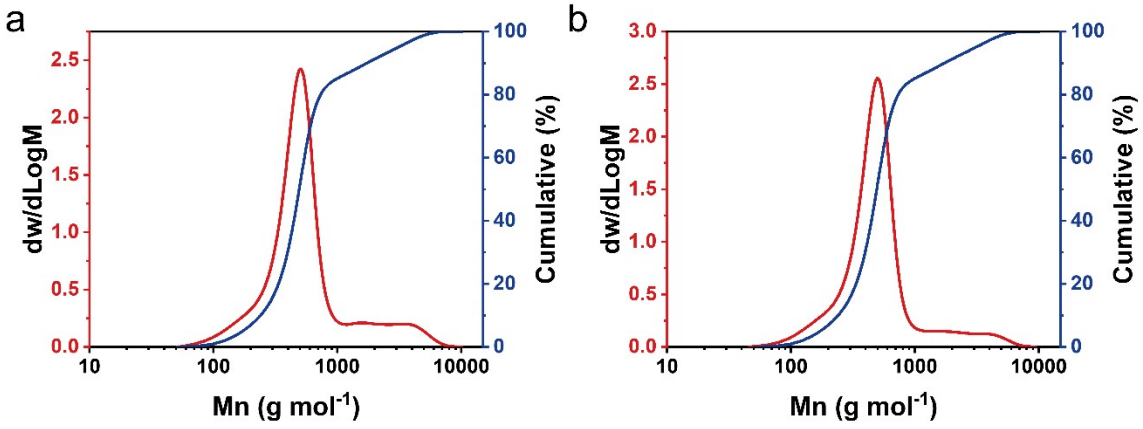

Figure S8. GPC curves of (a) PDND/C and (b) PDND/I.

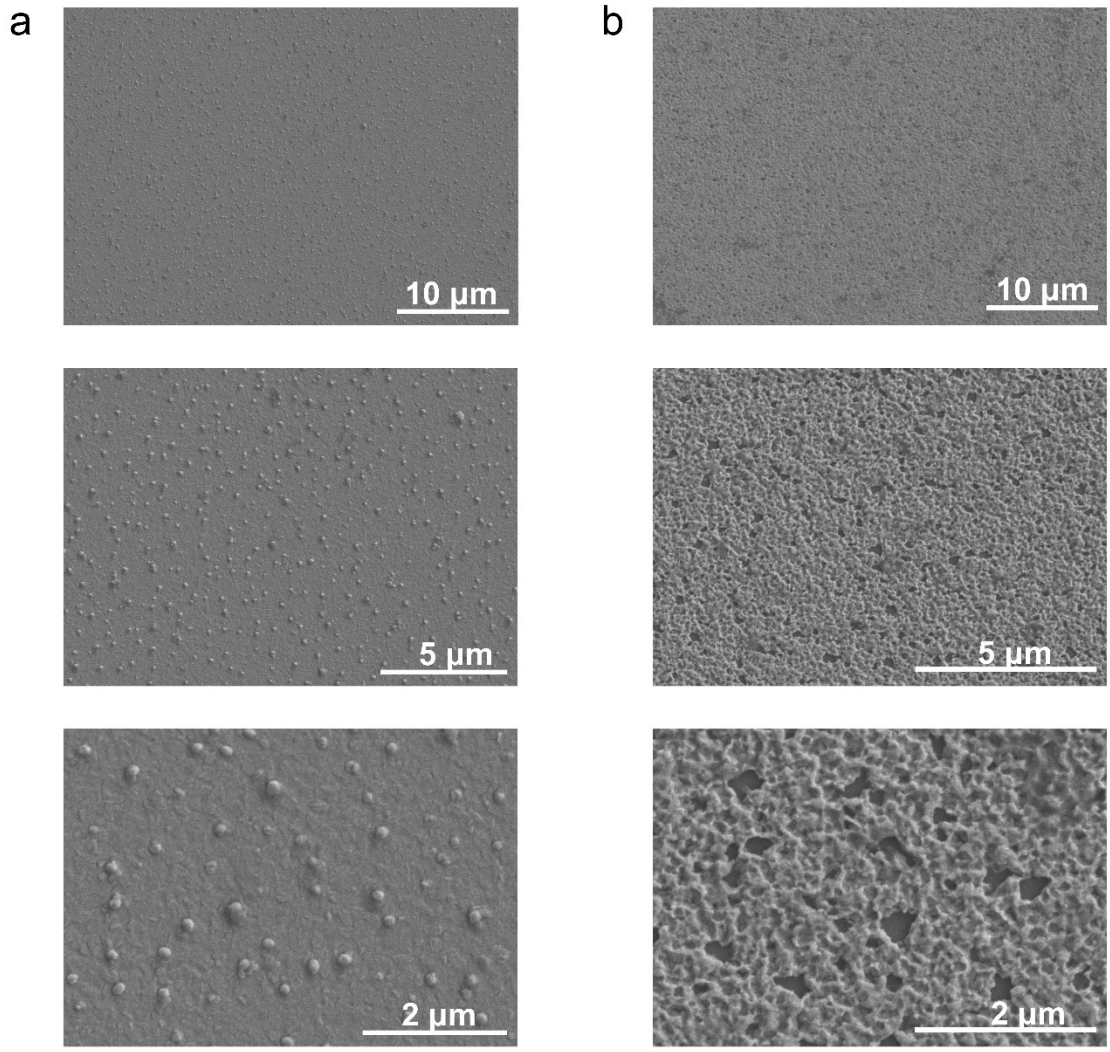

Figure S9. SEM of ITO surface (a) before and (b) after electropolymerization.

As illustrated in **Figure S9**, after completion of the electropolymerization reaction, the surface of the ITO substrate exhibits an obvious etched morphology, which is similar to the honeycomb pore structure. This degradation of the substrate significantly impairs the charge transfer efficiency during the electropolymerization process, thereby reducing the degree of polymerization.

Figure S10. Photographs of the PDND-soaked electrolyte (1 M $Al(ClO_4)_3$) for different time intervals.

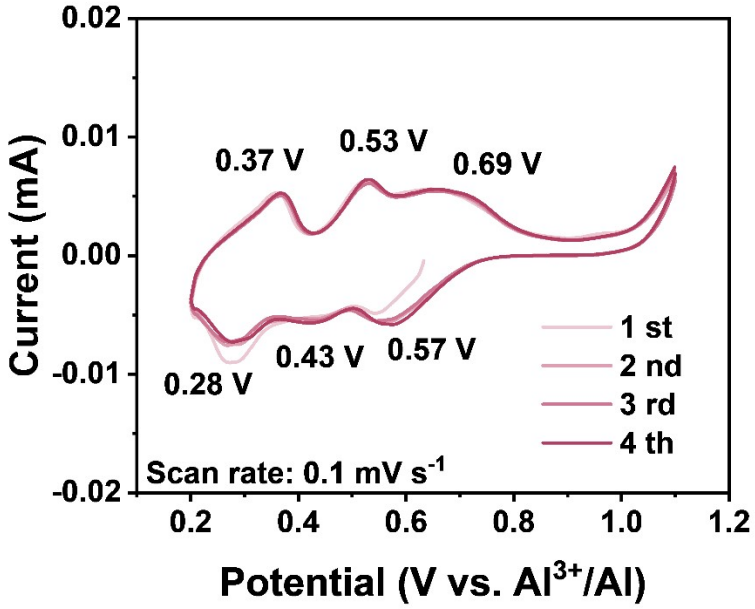

Figure S11. CV curves of the Al//PDND-I battery at a scan rate of 0.1 mV s

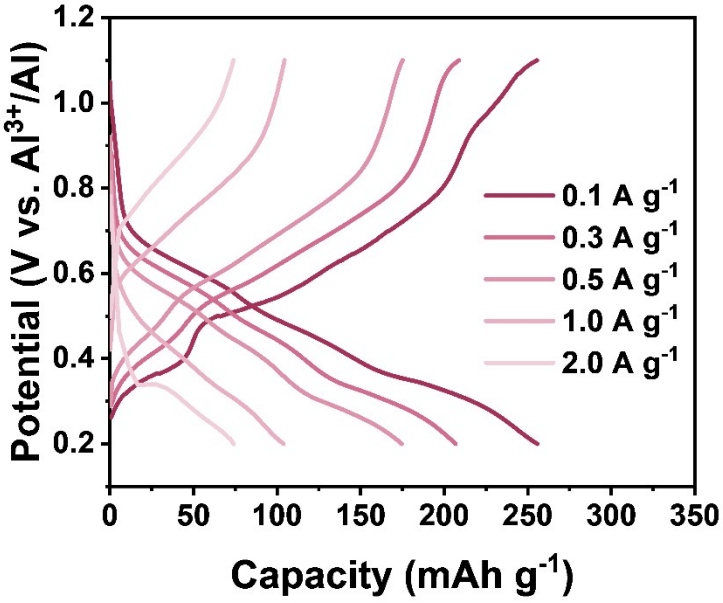

Figure S12. Charge/discharge profiles of Al//PDND/I battery at different rates.

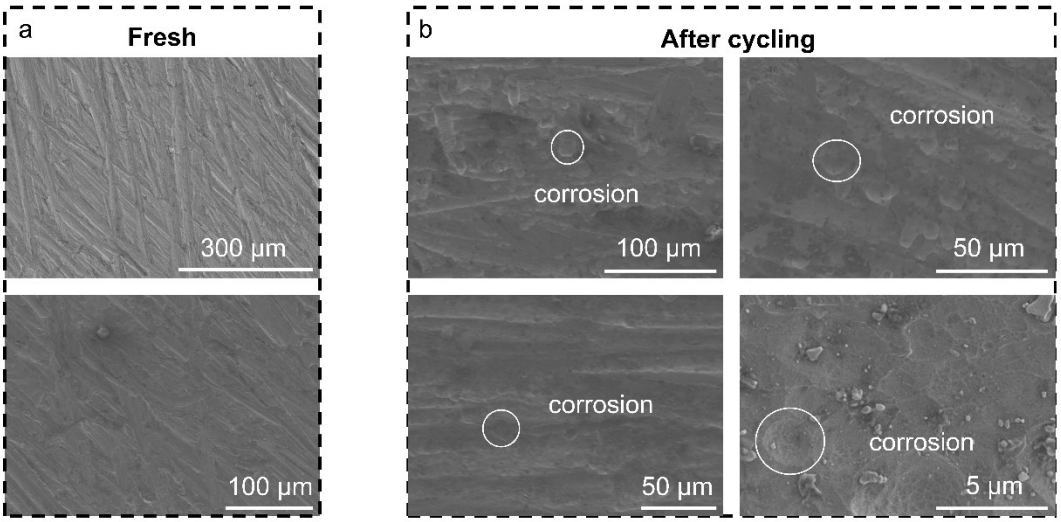

Figure S13. SEM images of (a) the fresh anode and (b) the post-mortem anode.

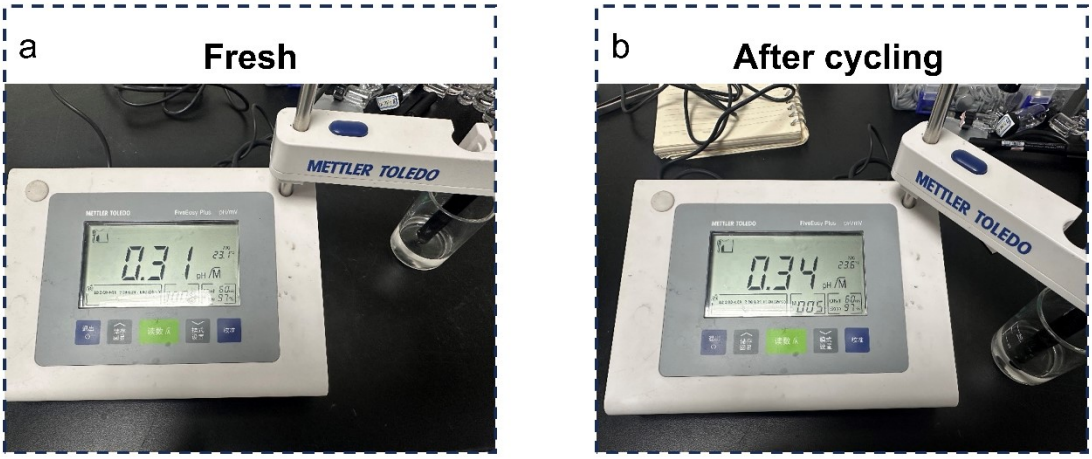

Figure S14. The pH of the $Al(ClO_4)_3$ electrolyte (a) before and (b) after 100 cycling.

The electrolyte pH remained remarkably stable, shifting only slightly to 0.34 after 100 cycling, indicating no severe pH drift.

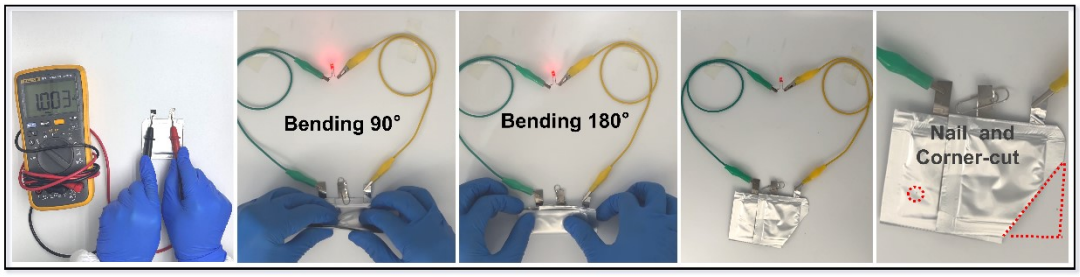

Figure S15. The extreme test of the Al//PDND/C soft-package battery

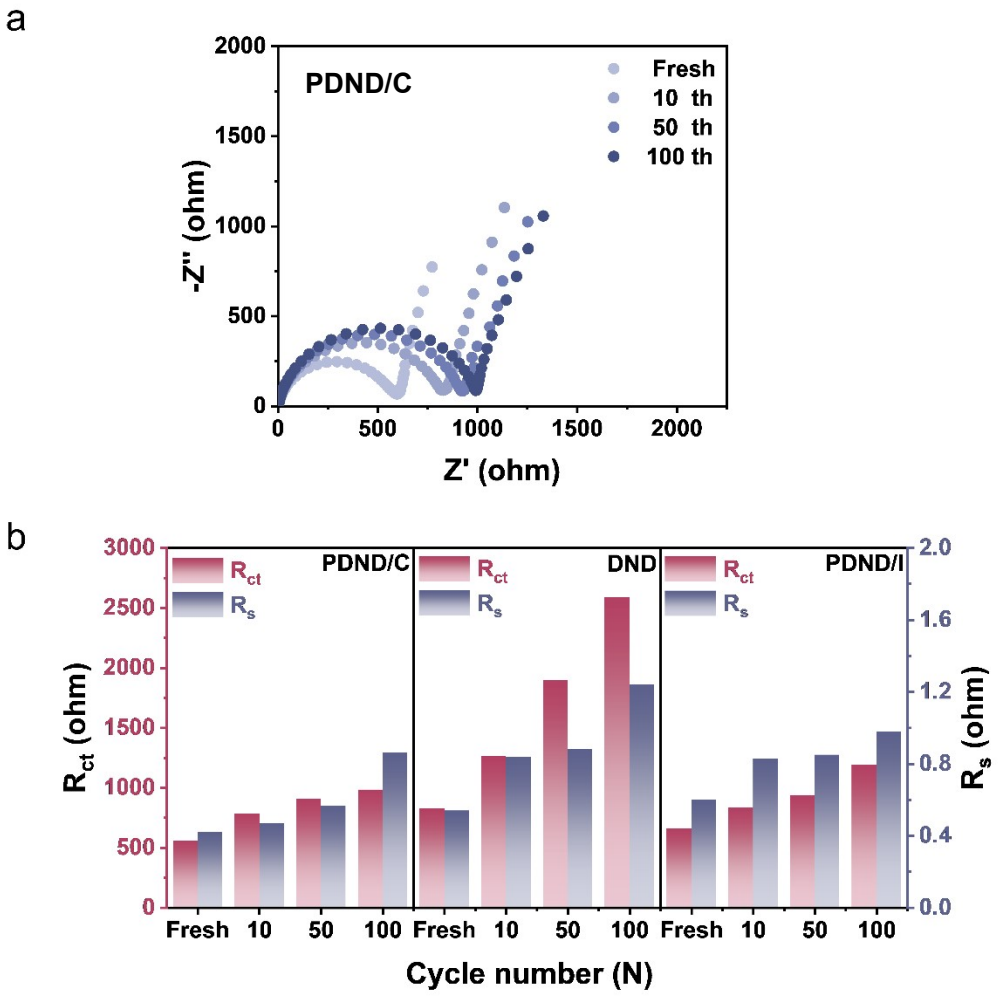

Figure S16. The calculated R_{ct} and R_s of PDND/C, DND, and PDND/I cathodes after different cycles.

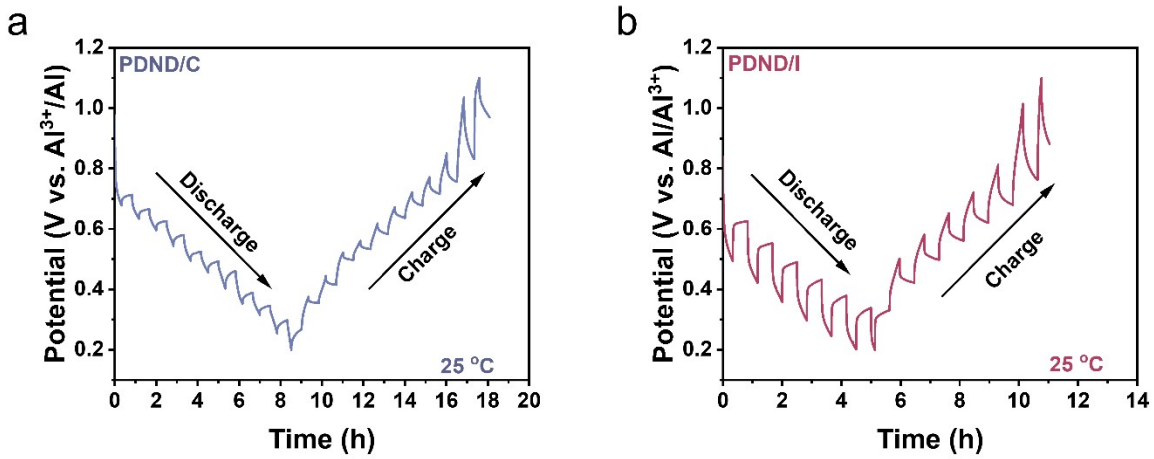

Figure S17 GITT curves of (a) PDND/C and (b) PDND/I cathodes

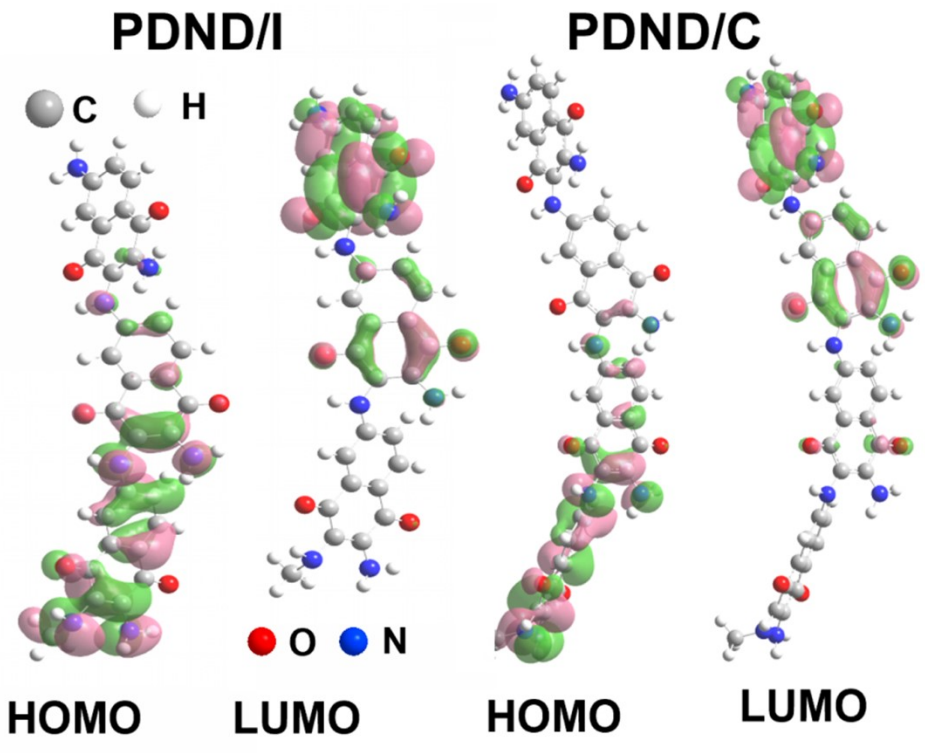

Figure S18. HOMO and LUMO of the optimized PDND/C and PDND/I models.

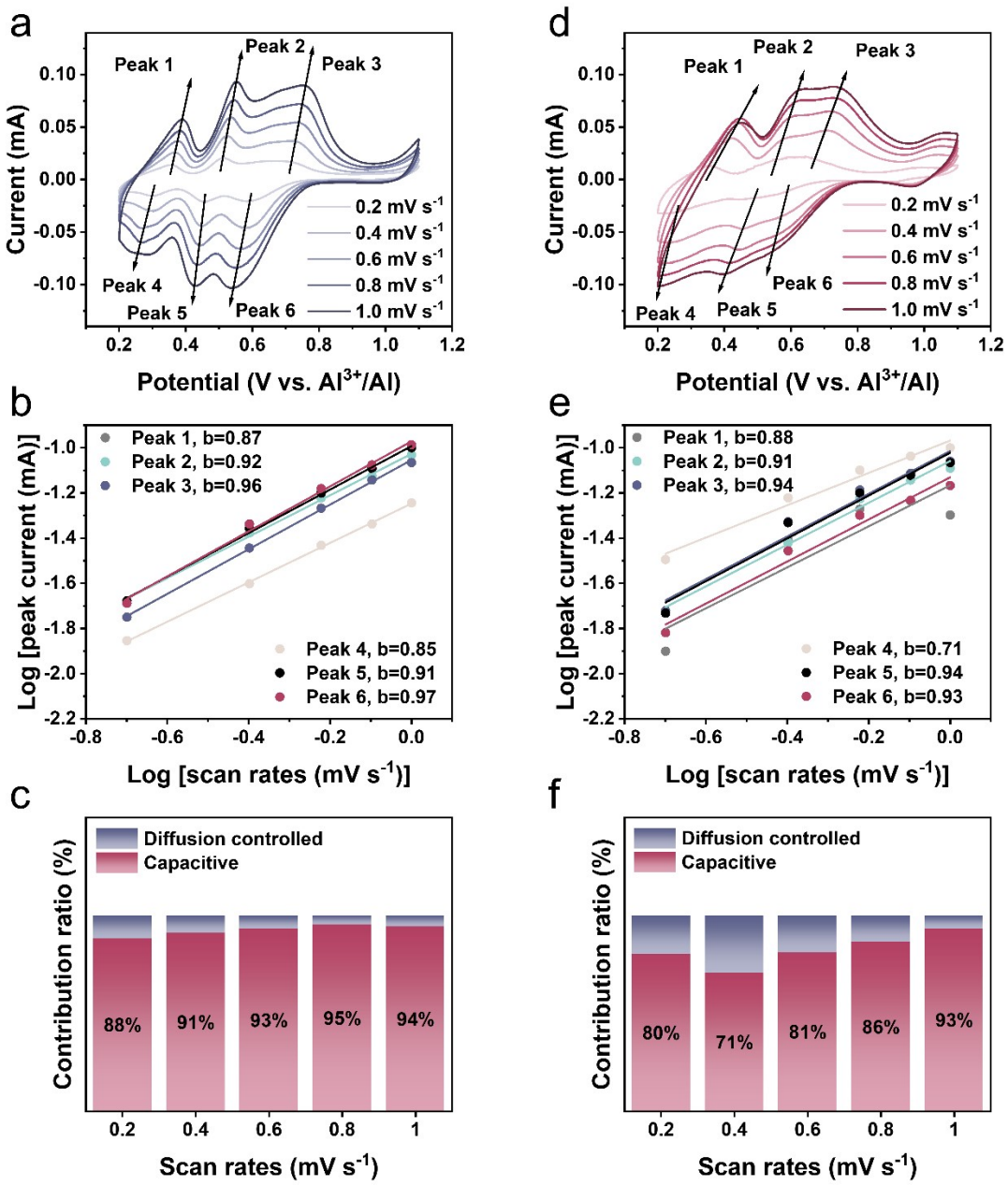

Figure S19. CV curves of (a) PDND/C and (d) PDND/I at different scan rates. The relationship between redox peak current and scan rate for (b) PDND/C and (e) PDND/I cathode from CV curves. The capacitive and diffusion contributions for (c) PDND/C and (f) PDND/I cathodes at various scan rates.

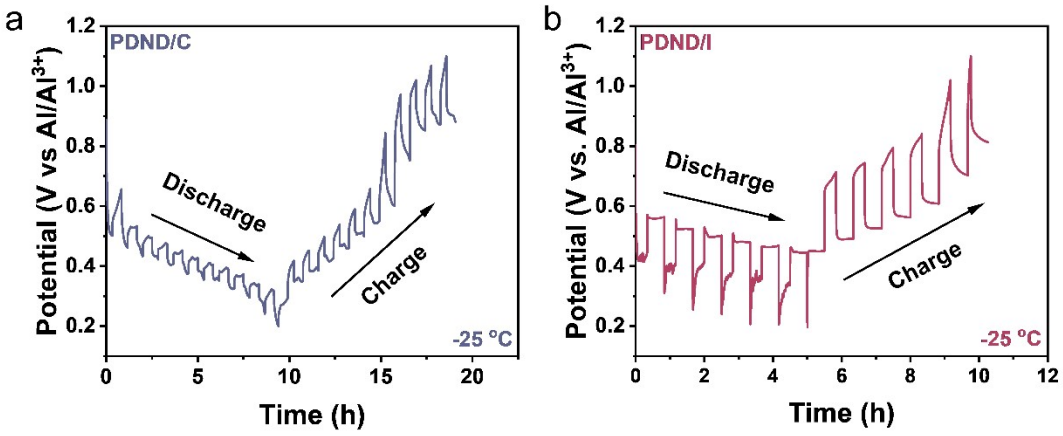

Figure S20. GITT curves of (a) PDND/C and (b) PDND/I cathodes at -25 °C.

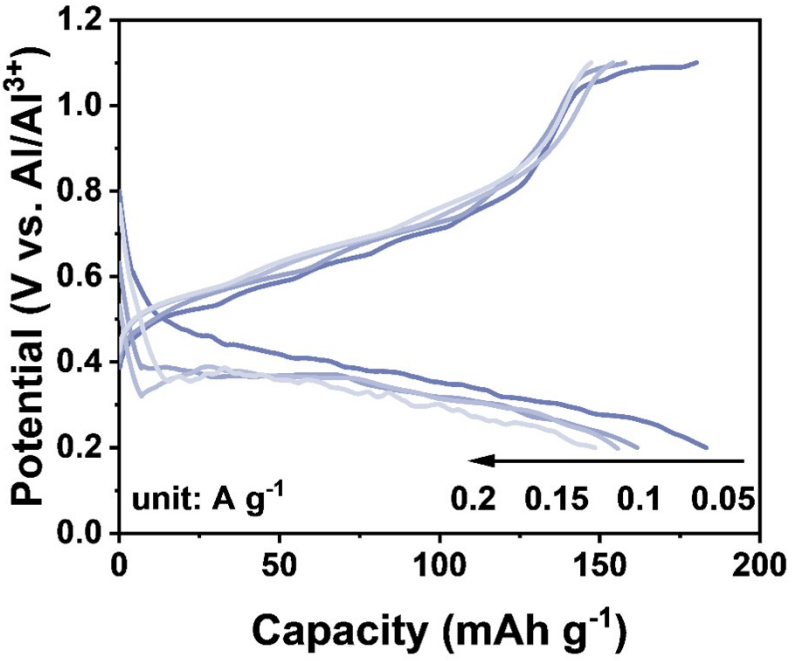

Figure S21. Charge/discharge profiles of Al//PDND/C battery at different rates at -25 °C.

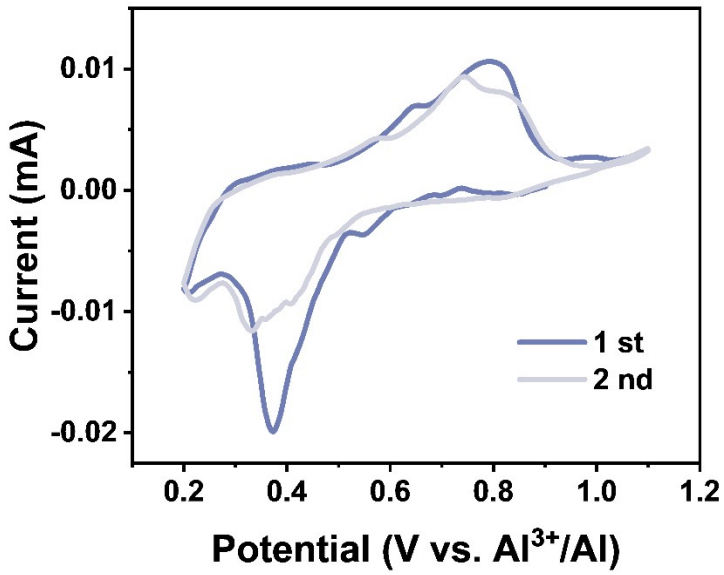

Figure S22. CV curves of Al//PDND/C battery at -25 °C.

Increased electrolyte viscosity (**Figure S22**) hinders ion migration, causing multiple redox peak pairs to merge into broadened peaks. Notably, the material's electrochemical performance remains stable under low-temperature conditions.

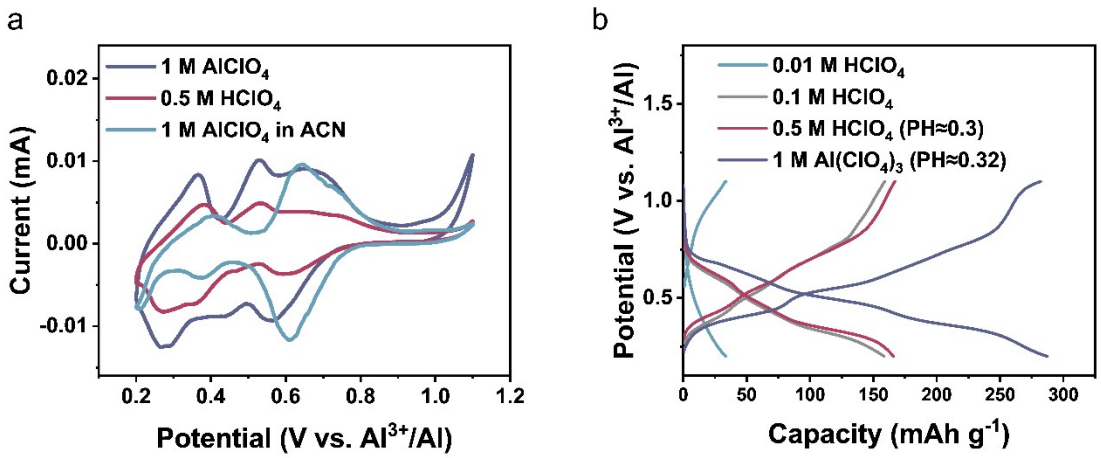

Figure S23. (a) CV curves and (b) charge/discharge profiles of Al//PDND/C battery with different electrolytes.

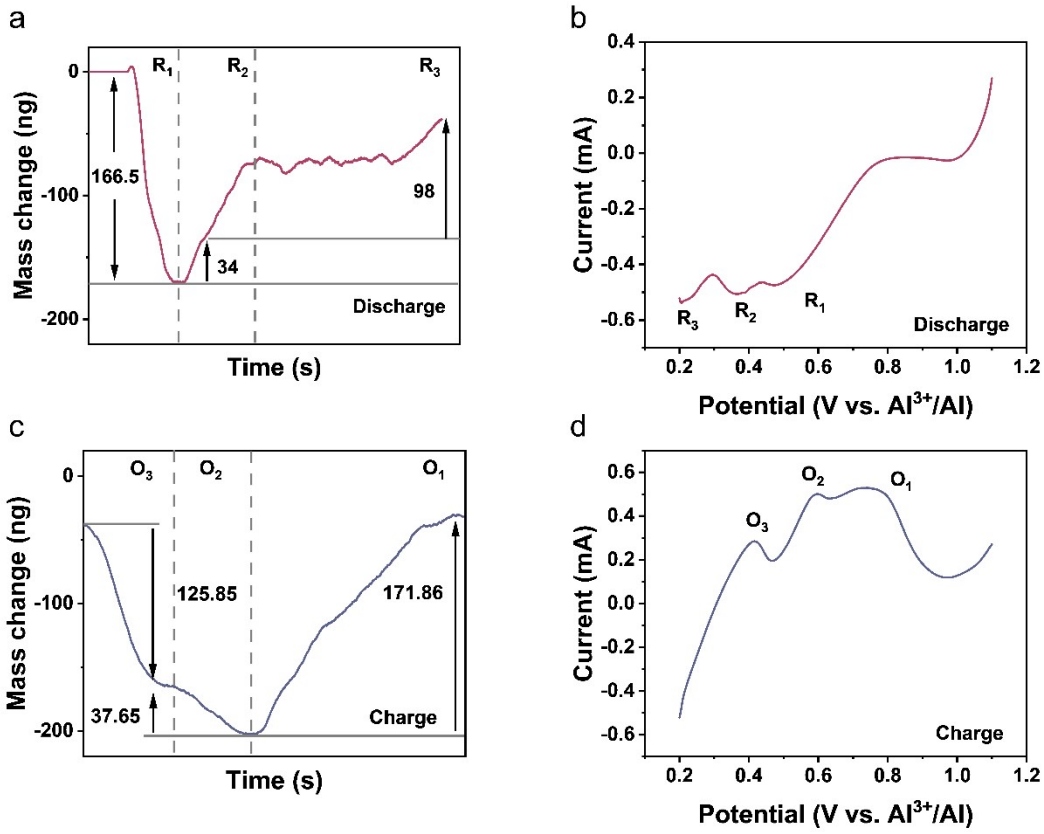

Figure S24. *Operando* EQCM-D test for the PDND cathode during the (a, b) discharging and (c, d) charging processes.

Operando EQCM-D measurements: The measurement of mass changes during electrochemical reaction was conducted using an *operando* EQCM-D with a Biolin Scientific Qsense Analyzer. This technique aims to obtain the ratio of mass changes to charge transfer (Δm/Δq), which is calculated by the following Faraday's law.

$$\frac{\Delta m}{\Delta q} = \frac{\Delta m}{nF}$$

Where Δm stands for the mass change (g), Δq stands for the charge transfer (C), F is the Faraday constant (96485 C mol^{-1}), and n is the electron transfer number.

The theoretical capacity of Al^{3+} to react with PDND is calculated based on the following equation:

$$\frac{\Delta m}{\Delta q} = \frac{\Delta m}{nF} = \frac{27}{3 \times 96485} mg/C = 0.093\ mg/C$$

The theoretical capacity of H_3O^+ to react with PDND is calculated based on the

following equation:

$$\frac{\Delta m}{\Delta q} = \frac{\Delta m}{nF} = \frac{19}{1 \times 96485} mg/C = 0.197\ mg/C$$

The theoretical capacity of ClO_4^- to react with PDND is calculated based on the following equation:

$$\frac{\Delta m}{\Delta q} = \frac{\Delta m}{nF} = \frac{99}{1 \times 96485} mg/C = 1.026\ mg/C$$

Combined with theoretical calculation and experimental measurements (**Figure S24** and **Table S1**), numerical analysis of the charge-to-mass ratio shows that ClO_4^- is preferentially extracted during the discharge process (R_1). The R_2 reduction peak corresponds to the insertion of H_3O^+, and the final reduction peak (R_3) is attributed to the insertion of Al^{3+}. During charging, three oxidation peaks are observed: O_3 (extraction of Al^{3+}), O_2 (extraction of H_3O^+), and O_1 (reinsertion of ClO_4^-), respectively. This phenomenon further confirms the $Al^{3+}/H^+/ClO_4^-$ triple co-storage mechanism in the PDND cathode.

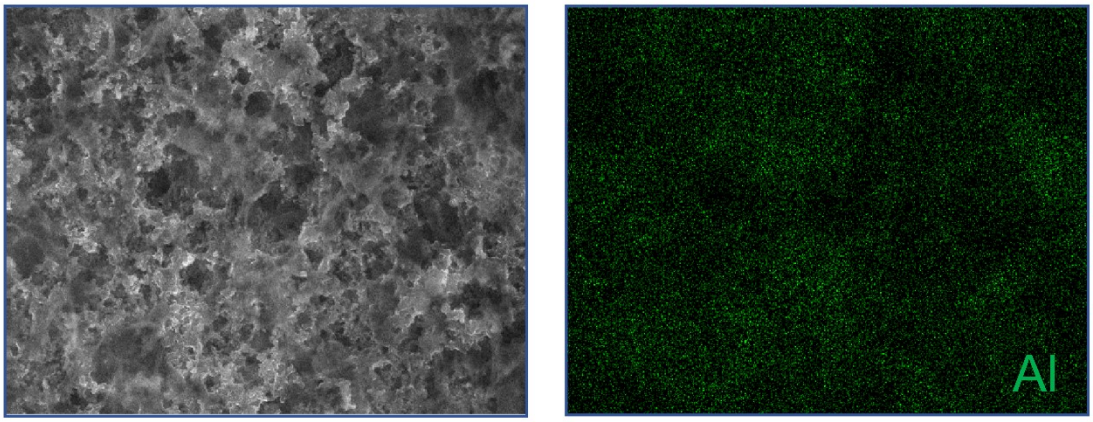

Figure S25. SEM and corresponding elemental mapping images of the fully discharged PDND cathode.

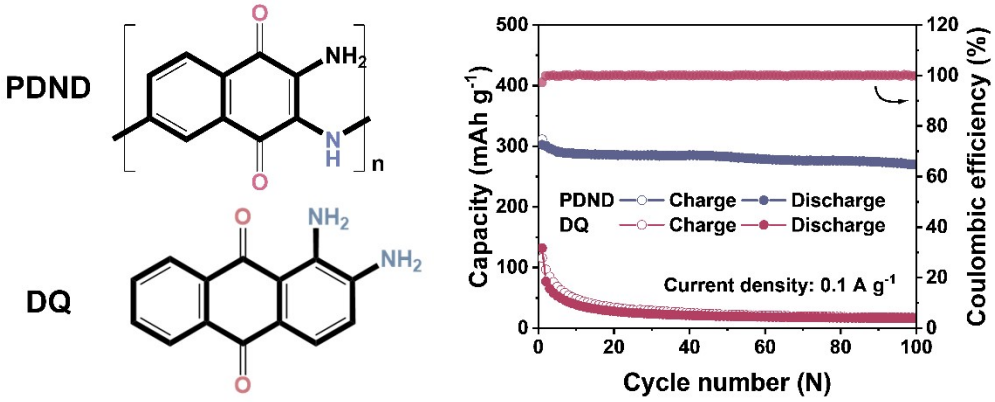

Figure S26. Cycling performance of PDND and DQ at a current density of 0.1 A g^{-1}

As shown in **Figure S26**, the PDND cathode demonstrates significant advantages over the analogous quinone-based electrodes such as 2,6-diaminoanthraquinone (DQ). The PDND cathode delivers a higher capacity of 302 mAh g^{-1} and superior cycling stability. Notably, the Al//PDND battery using a standard electrolyte (without antifreeze additives) operates even at −25 °C, whereas the Al//DQ battery fails under identical conditions. These results collectively underscore the distinctive structural design of PDND and its resultant performance advantages.

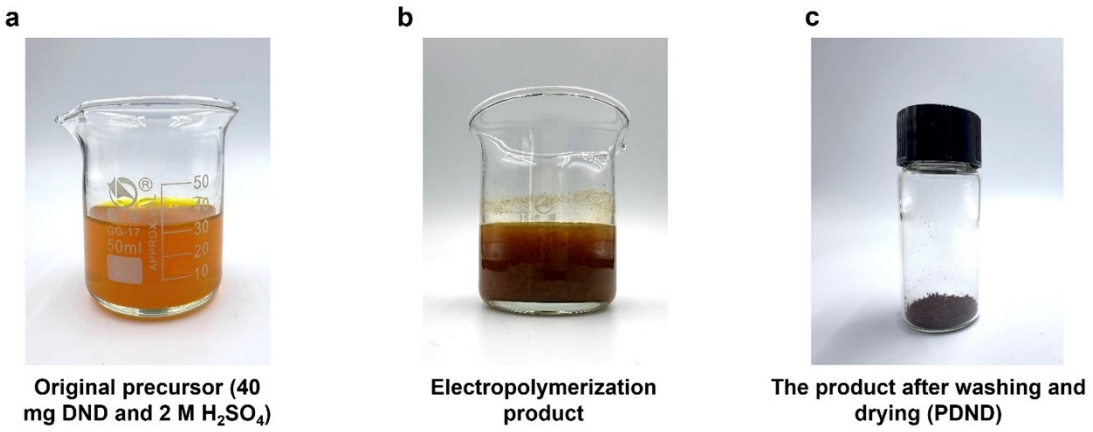

Figure S27. The precursor, reaction effluent, and the target product of the electropolymerization.

First, the reaction mixture (**Figure S27a**) was continuously pumped into the continuous-flow electrochemical reactor with an injection pump. Meanwhile, the electropolymerization reaction was carried out by cyclic voltammetry (scan rate: 50 mV s^{-1}, potential window: −0.4 to 1.2 V). This process occurs via the oxidative coupling of the $–NH_2$ groups on DND, forming –NH– linkages that extend the polymer backbone. After the reaction was stabilized, the reaction effluent was collected and separated by centrifugation (**Figure S27b**). Finally, the target powder (PDND, **Figure S27c**) was obtained after being further washed with water and acetonitrile to remove impurities, followed by vacuum drying.

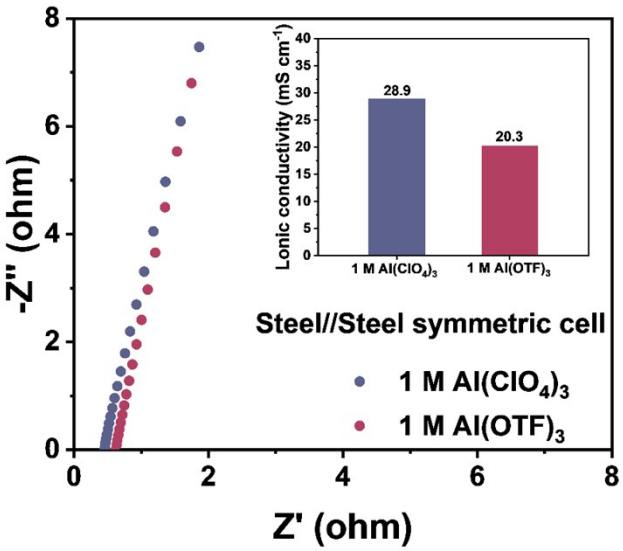

Figure S28. EIS plots of the steel//steel symmetric cell with different electrolytes.

The ionic conductivity of the 1 M $Al(ClO_4)_3$ electrolyte (28.9 mS cm^{-1}) is higher than that of the 1 M $Al(OTf)_3$ electrolyte (20.3 mS cm^{-1}). In this case, the ionic diffusion kinetics in $Al(ClO_4)_3$ electrolyte are superior to those in the 1 M $Al(OTf)_3$ electrolyte (**Figure S28**).

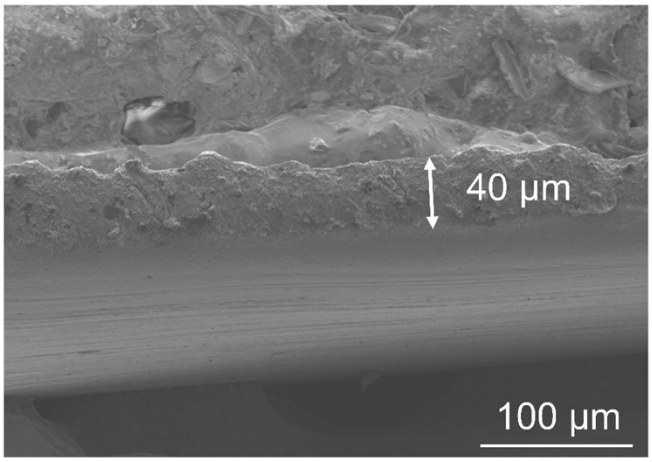

Figure S29. SEM image of the PDND cathode.

Comment [cz]: 这个图 在 Res Lett 里面 没有提及，是正文中有吗？

Comment [CJ]: 第二个审稿人的问题 2-1

Table S1. The data of Δm, Δe and Δm/e for each step of the redox reaction.

	Δm(ng)	**Δe (μC)**	**Δm/e (mg/C)**
R_1	166.5	168	0.99
R_2	34	191	0.178
R_3	98	940	0.104
O_3	125.85	1063	0.11
O_2	37.65	225.67	0.17
O_1	171.86	168	1.023